Journal of Inorganic Biochemistry 282 (2026) 113350

Contents lists available at ScienceDirect

Journal of Inorganic Biochemistry

journal homepage: www.elsevier.com/locate/jinorgbio

Nickel binding shifts *Helicobacter pylori* HypA toward compact conformations☆,☆☆

Stefano Ciurli [a,*], Luca Mazzei [a], Barbara Zambelli [a], Sofia Ranieri [a], Noemi Carosella [a], Massimo Lucci [b], Frans A.A. Mulder [c]

[a] *Laboratory of Bioinorganic Chemistry, Department of Pharmacy and Biotechnology, University of Bologna, Bologna, Italy*
[b] *CIRMMP, University of Florence, Sesto Fiorentino, Florence, Italy*
[c] *Institute of Biochemistry, Johannes Kepler University, Linz, Austria*

ARTICLE INFO

Keywords:
Helicobacter pylori
HypA
Nickel metallochaperone
NMR spectroscopy
Protein dynamics
Model-free analysis
Rotational diffusion

ABSTRACT

Helicobacter pylori (*Hp*) is a Gram-negative human pathogen that relies on the nickel enzymes urease and [Ni,Fe]-hydrogenase for gastric colonization. Delivery of Ni(II) to the active sites of these enzymes is mediated by the metallochaperone *Hp*HypA, which contains a high-affinity structural Zn(II) site and a lower-affinity Ni(II) site, in two distinct domains. Although the NMR solution structure of the apo form Zn-*Hp*HypA is known, the impact of Ni(II) binding on the structure remains unclear. Here, NMR ^{15}N relaxation experiments have been applied to probe the backbone internal dynamics and the rotational diffusion of Zn-*Hp*HypA and Ni,Zn-*Hp*HypA. Residue-resolved model-free analysis revealed broadly similar ps–ns backbone motional amplitudes in the apo and holo states. In contrast, Ni(II) binding increased rotational diffusion, indicating a reduced hydrodynamic radius and a shift toward a more compact conformational ensemble. These observations support a model in which Ni(II) binding generates a delivery-competent protein structure by narrowing the accessible conformational distribution during partner recognition. Previously, calorimetric data reported on the interaction between *Hp*HypA and the urease metallochaperone homodimeric *Hp*UreE$_2$, which showed micromolar Ni(II) binding to *Hp*HypA but the emergence of a sub-nanomolar, strongly exothermic Ni site in the HypA•UreE$_2$ complex. The observed nickel-induced ensemble compaction determined by solution NMR spectroscopy provides a plausible physical basis for Ni-dependent conformational switching to promote high-affinity protein-protein recognition.

1. Introduction

Nickel is an essential cofactor for several enzymes in *Helicobacter pylori* (*H. pylori*, *Hp*) [1–5], most notably urease and [Ni,Fe]-hydrogenase, which are critical for the bacterial colonization and persistence within the gastric mucosa [6–10]. The centrality of Ni(II) to these pathways creates a stringent homeostatic challenge: intracellular free nickel is both scarce and potentially toxic [11], so that *H. pylori* must couple nickel acquisition to highly controlled intracellular trafficking, buffering, and targeted delivery to enzyme maturation systems [12–25]. The logic of minimizing uncontrolled Ni(II) reactivity while ensuring efficient transport to the correct proteins implies that nickel metabolism in *H. pylori* is governed not only by thermodynamics, through the protein-metal ion affinity, but also by kinetic control and regulation of macromolecular interactions dynamics.

A central component of this metal-trafficking network is *H. pylori* HypA (*Hp*HypA), a nickel metallochaperone required for assembly of both urease and [Ni,Fe]-hydrogenase [10,12–14,26–28]. In particular, *Hp*HypA interacts with the homodimeric nickel chaperone UreE$_2$, involved in the activation pathway of urease, and with the large subunit HyhL of the hydrogenase heterodimer [10], and is thus placed at a crossroad for the activation of key enzymes for *H. pylori* metabolism.

*Hp*HypA contains two metal sites with distinct roles (Fig. 1): a high-affinity structural Zn(II) site, made of four conserved cysteine residues that stabilizes the protein fold, and a distinct, lower-affinity Ni(II) site associated with nickel delivery to downstream maturation partners and

☆ This article is part of a Special issue entitled: 'Harry Gray Special Issue' published in Journal of Inorganic Biochemistry.
☆☆ Given his role as Editor-in-Chief, Stefano Ciurli had no involvement in the peer review of this article and had no access to information regarding its peer review. Full responsibility for the editorial process for this article was delegated to another journal editor.

* Corresponding author.
E-mail address: stefano.ciurli@unibo.it (S. Ciurli).

https://doi.org/10.1016/j.jinorgbio.2026.113350
Received 28 March 2026; Received in revised form 25 April 2026; Accepted 2 May 2026
Available online 5 May 2026

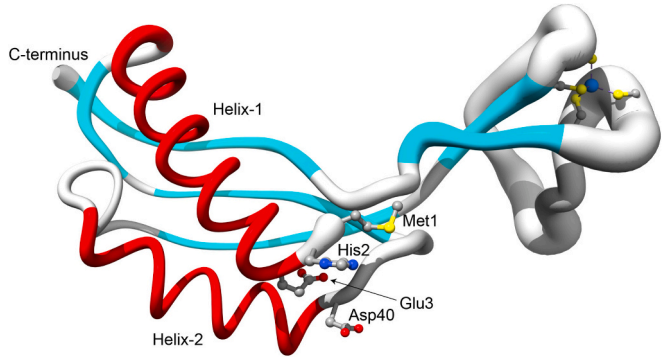

Fig. 1. Structure of Zn-*Hp*HypA. The protein is shown as a "sausage" representation of the NMR ensemble (PDB code: 6G81), colored by secondary structure elements (α-helices colored red, β-strands colored cyan, and loops/turns in white/gray). Tube thickness is scaled to residue specific RMSD of the Cα atoms. The structural Zn(II) ion is shown as a blue sphere and coordinating Cys74, Cys77, Cys91, and Cys94; the Ni(II)-binding residues Met1, His2, Glu3, and Asp40 are also shown (side chains shown as ball-and-stick and colored according to the CPK code). The position of helix-1 and helix-2 is also indicated. Figure made with Chimera [33]. (For interpretation of the references to colour in this figure legend, the reader is referred to the web version of this article.)

eventually to the target enzymes [29–32]. While the solution structure of wild-type apo Zn-*Hp*HypA has been determined [31] the structural and dynamic consequences of Ni(II) binding to obtain the holo form (Ni,Zn-*Hp*HypA) remain unclear. Therefore, understanding how Ni(II) binding influences the structure and dynamics of *Hp*HypA is crucial for elucidating its mechanism of nickel delivery. Site-directed mutagenesis experiments coupled with spectroscopic evidence indicate that the amine N atom of Met1, the amide N atom of His2 and Glu3, as well as the side chain imidazole N of His2 and the carboxylate O atoms of Glu3 and Asp40 (the latter residue located on the beginning of helix-2 facing the N-terminus), are the residues composing the Ni(II)-site in wild-type *Hp*HypA [13,27,28,31] (Fig. 1).

Delivery of Ni(II) is necessarily a transient, multi-step process: Zn-*Hp*HypA must bind Ni(II), avoid off-pathway sequestration, engage specific partners, and promote metal transfer without globally destabilizing its fold. This logic parallels the stepwise, intermediate-mediated transfer mechanisms and enthalpy–entropy compensation described for other metallochaperone systems such as, for example, involved in copper trafficking [34–37] and nickel-dependent transcription regulation [38,39]. These steps imply the existence of an ensemble-based mechanism in which the protein samples multiple substates that differ in metal coordination geometry, accessibility of ligands, and engaging of interaction surfaces, with metal binding redistributing these populations toward delivery-competent configurations while tuning the enthalpy/entropy partitioning of subsequent recognition and transfer steps [36,40–42]. Therefore, the relevant question is how Ni(II) binding reshapes the energy landscape of Zn-*Hp*HypA to balance stability with the controlled plasticity needed for protein-protein interactions, potentially by modulating conformational populations and internal dynamics while redistributing enthalpic and entropic contributions to binding [36,40–48].

Solution NMR spectroscopy is uniquely positioned to address this problem because it can explore proteins as dynamic molecules in solution, providing residue-specific observables that connect structural fingerprints to motion over a wide range of timescales [43,49,50] and, critically, enabling quantitative links between internal dynamics and conformational entropy contributions to molecular recognition [46–48,51]. Chemical shifts [52] and line shapes [50] sensitively detect changes in local environments and population redistribution even when the overall fold is largely maintained, whereas nuclear spin relaxation measurements quantify the motional degrees of freedom that underlie conformational selection, induced fit, and exchange between substates [40–42,44,46]. In particular, backbone ^{15}N relaxation experiments (R_1, R_2, and ^{1}H—^{15}N *NOE*) probe internal motions in the pico-to-nanoseconds time scale through their dependence on the spectral density function, and can also detect micro-to-milliseconds conformational exchange contributions that often accompany binding-competent interconversions [50,53–55]; these relaxation-derived parameters provide a practical route to mapping changes in internal flexibility and estimating corresponding shifts in conformational entropy [46–48,51]. Moreover, these observables provide means for separating internal dynamics from overall tumbling and for defining global rotational diffusion parameters, enabling a joint description of local flexibility and molecular hydrodynamics [50,51,56,57]. Backbone ^{15}N relaxation probes motions across a broad range of timescales: R_1 predominantly reflects molecular motions in the *fast* timescale (ps-ns), corresponding to frequencies near the ^{15}N Larmor frequency (ω_N), whereas R_2 is sensitive to both *fast* motions and *slow* (μs-ms) processes, including chemical exchange (R_{ex}); steady-state heteronuclear NOEs are sensitive to very fast motions and decrease in the presence of *fast* (nanosecond) dynamics and even *faster* (picosecond) fluctuations [58,59]. The combined analysis of R_1, R_2, and *NOE* therefore provides a comprehensive view of backbone mobility from picoseconds to milliseconds.

In this study, these strengths of NMR spectroscopy were used to quantify how Ni(II) binding influences the conformational ensemble, dynamics, and hydrodynamic properties of Zn-*Hp*HypA. ^{15}N relaxation data for both Zn-*Hp*HypA and Ni,Zn-*Hp*HypA were analyzed using the extended Lipari-Szabo model-free formalism together with rotational diffusion tensor optimization to obtain residue-specific order and global tumbling parameters. By integrating residue-level dynamics information with global rotational diffusion behavior, this approach revealed how Ni(II) binding modulates the dynamics of *Hp*HypA by inducing a more compact protein conformational ensemble without altering the internal dynamics. These observations support a model in which metal-induced conformational selection enhances the specificity and efficiency of Ni(II) trafficking in *H. pylori*, thus providing a mechanistic framework for understanding how *H. pylori* achieves specific and efficient Ni(II) delivery to urease and [Ni,Fe]-hydrogenase despite metal scarcity and toxicity.

2. Materials and methods

2.1. Protein production and purification

Uniformly ^{15}N-labeled Zn-*Hp*HypA ([U—^{15}N] Zn-*Hp*HypA) was expressed and purified as previously described [31]. NMR samples contained *ca.* 1 mM [U—^{15}N] Zn-*Hp*HypA in 20 mM HEPES (pH 7.2), 200 mM NaCl, 1 mM TCEP, and 10% D_2O ("NMR buffer"). For holo samples, 1.1 equivalents of Ni(II) were added to Zn-*Hp*HypA as a concentrated $NiSO_4$ solution in the same buffer. Samples were flash-frozen in liquid nitrogen, stored at −80 °C, and thawed immediately before measurement. Throughout this work, the term Zn-*Hp*HypA (apo) refers to the purified protein containing one equivalent of Zn(II) and no other metal ions, as verified by inductively coupled plasma optical emission spectroscopy (ICP-OES) using a previously described method [60]. The term Ni,Zn-*Hp*HypA (holo) denotes the protein additionally bound to one Ni(II) equivalent.

2.2. Determination of ^{15}N relaxation parameters

Backbone ^{15}N NMR relaxation experiments were performed to determine longitudinal ($R_1 = 1/T_1$) and transverse ($R_2 = 1/T_2$) relaxation rates, together with the steady-state heteronuclear ^{1}H—^{15}N NOE (denoted NOE hereafter). Data were acquired for both Zn-*Hp*HypA and Ni,Zn-*Hp*HypA at 16.44 T (corresponding to a LArmor frequency of 700.13 MHz). All experiments employed phase-sensitive pulse sequences using gradient coherence selection (echo/antiecho-TPPI) with proton decoupling during acquisition [54,58]. Specifically, R_1, R_2, and

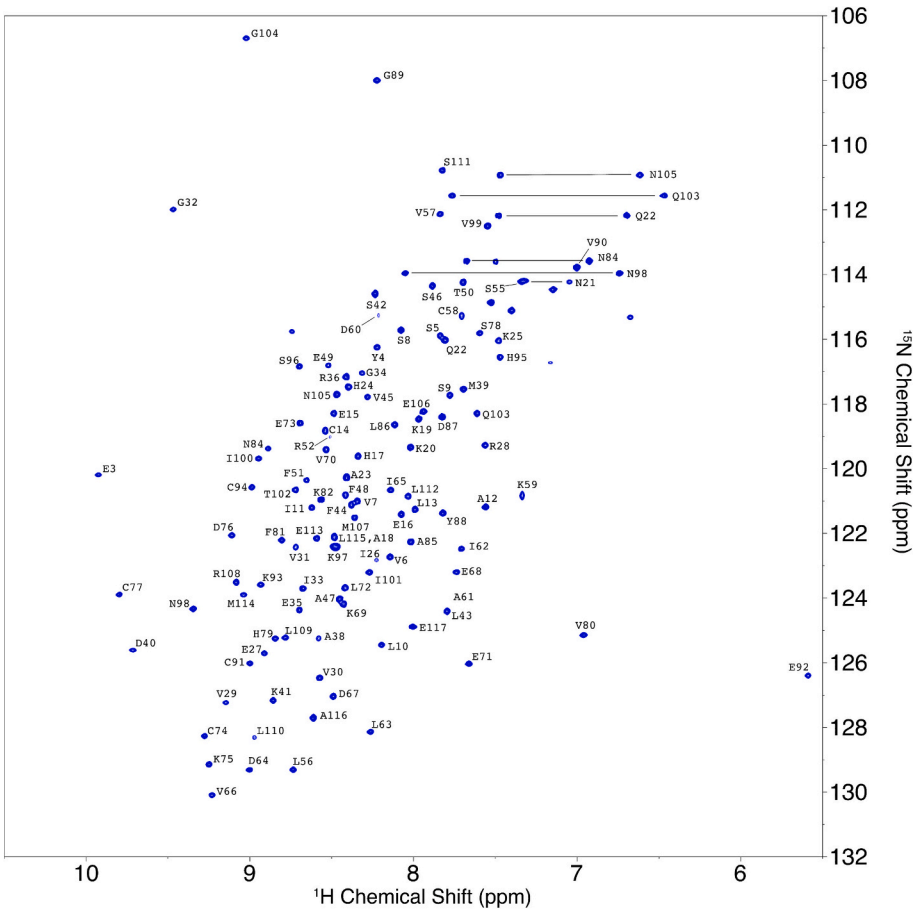

Fig. 2. $^{1}H,^{15}N$ HSQC spectrum of apo-*Hp*HypA at 900 MHz at pH 7.2. The spectrum shows the relative positions of the peaks, each representing a N—H pair of the amides in the protein main chain. Assignments of individual peaks are shown as labels containing the single letter amino acid code and the corresponding residue number. The peak positions are relative to the ^{1}H and ^{15}N chemical shift scales of the ω1 and ω2 dimensions, respectively (ppm scales). The pairs of signals corresponding to the amide groups of glutamine/asparagine residues are also shown, with lines linking the HD21/HE21 (left peak) and the HD22/HE22 (right peak) proton signals.

NOE data were collected, respectively, using the Bruker pulse programs hsqct1etf3gpsi.2 (which employs ^{1}H 180° pulses in place of continuous wave composite pulse decoupling), hsqct2etf3gpsi.large (which allows delays as short as 8.48 ms and further incorporates temperature compensation blocks [61] to improve thermal stability and reproducibility by applying "no-load" CPMG–T_2 cycles for all delays shorter than the longest one acquired, thereby equalizing the RF duty cycle across the entire experiment set), and hsqcnoef3gpsi. R_1 rates were obtained using ten relaxation delays from 10 to 1600 ms. R_2 rates were measured using Carr-Purcell-Meiboom-Gill (CPMG) spin-echo relaxation delays (ten points) ranging from 8.48 and 169.60 ms. For both R_1 and R_2 experiments, a recycle delay of 3.5 s was used. NOE values were obtained from paired HSQC spectra recorded with and without ^{1}H pre-saturation (3 s); a 6 s recycle delay was applied.

All spectra were processed with TopSpin 4.5.0 (Bruker) using a consistent set of parameters (window functions, zero-filling, apodization, phasing, and referencing). Published assignments for both Zn-*Hp*HypA and Ni,Zn-*Hp*HypA [31] were used. Peak intensities were extracted using Dynamics Center 2.8.8 (Bruker). R_1 and R_2 rates were obtained by fitting signal intensity decays to a two-parameter single-exponential model using a combination of Simplex and Levenberg-Marquard algorithms. Uncertainties were estimated by Monte Carlo simulations (95% confidence level). NOE values were calculated as the ratio of saturated to non-saturated spectral peak intensities; intensity uncertainties were derived from the standard deviation of the baseline noise.

2.3. Model-free analysis of NMR relaxation data

A quantitative analysis of backbone dynamics was performed to determine the amplitude and timescale of motions in both Zn-*Hp*HypA and Ni,Zn-*Hp*HypA. The analysis used the extended Lipari-Szabo model-free formalism [53,62,63] together with the Abragam-Redfield treatment of ^{15}N relaxation [64] (Eqs. 1–3). In this framework, the experimental observables R_1, R_2, and ^{1}H—^{15}N *NOE* are expressed as linear combinations of five spectral densities $J(\omega_i)$ (s), which quantify the intensity of motion-induced magnetic field fluctuations at $\omega = 0$, ω_H, ω_N, and $\omega_{H\pm}\omega_N$, and of an additional term R_{ex} (s^{-1}) that contributes to R_2 and accounts for μs–ms conformational-exchange broadening (Eqs. 1–3).

$$R_1\left(s^{-1}\right) = d[J(\omega_H - \omega_N) + 3J(\omega_N) + 6J(\omega_H + \omega_N)] + c[J(\omega_N)] \quad (1)$$

$$R_2\left(s^{-1}\right) = \frac{d}{2}[4J(0) + J(\omega_H - \omega_N) + 3J(\omega_N) + 6J(\omega_H) + 6J(\omega_H + \omega_N)] + \frac{c}{6}[4J(0) + 3J(\omega_N)] + R_{ex} \quad (2)$$

$$\frac{I}{I_0} = \eta = NOE = 1 + \frac{\gamma_H}{\gamma_N}\frac{\sigma_{NH}}{R_1}; \sigma_{NH} = d[6J(\omega_H + \omega_N) - J(\omega_H - \omega_N)] \quad (3)$$

In these expressions, d and c are the dipolar (^{1}H-^{15}N) and ^{15}N chemical shift anisotropy (CSA) interaction constants, respectively:

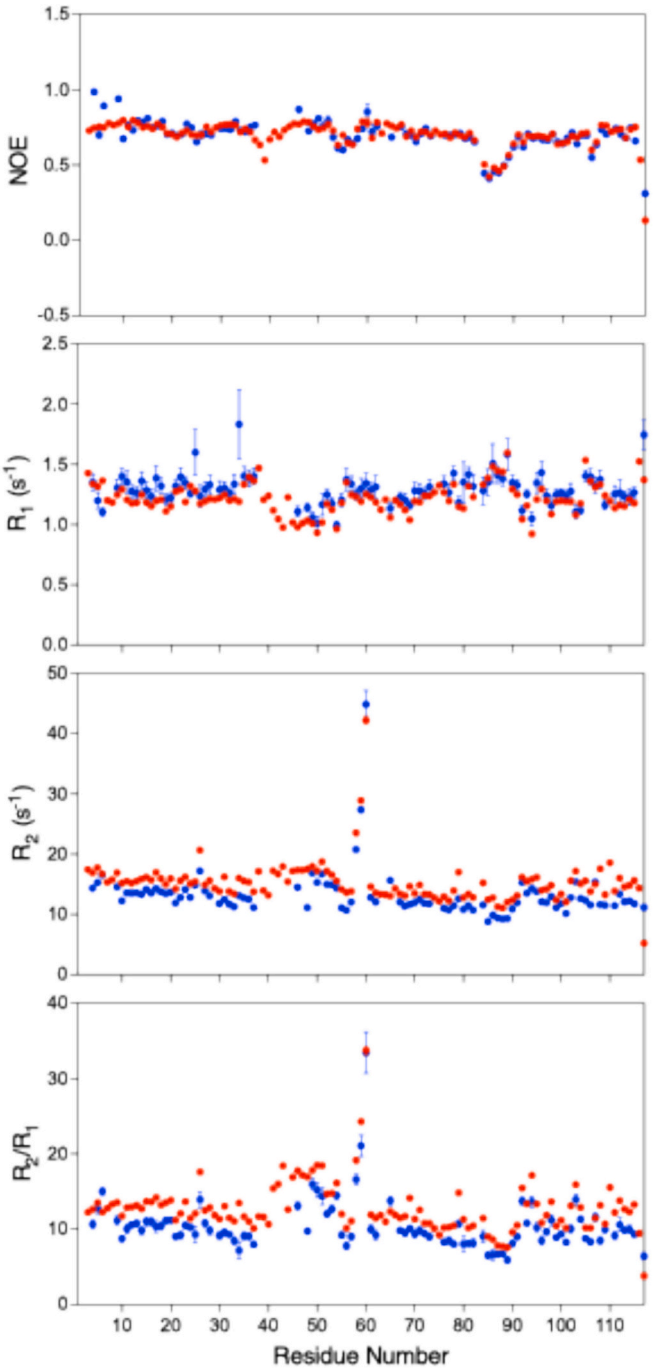

Fig. 3. Backbone ^{15}N relaxation parameters (NOE, R_1, R_2 and R_2/R_1) for Zn-*Hp*HypA (red dots) and Ni,Zn-*Hp*HypA (blue dots), measured at 16.4 T. Values are plotted along the *Hp*HypA sequence for assigned backbone amides. Error bars represent 95% confidence intervals from Monte Carlo analysis. Missing values correspond to unassigned or undetected resonances, including Ni(II)-proximal sites broadened in the holo state. (For interpretation of the references to colour in this figure legend, the reader is referred to the web version of this article.)

$$d\left(s^{-2}\right) = \frac{1}{4}\left(\frac{\mu_0}{4\pi}\right)^2 \frac{\gamma_H^2 \gamma_N^2 \hbar^2}{r_{NH}^6} \tag{4}$$

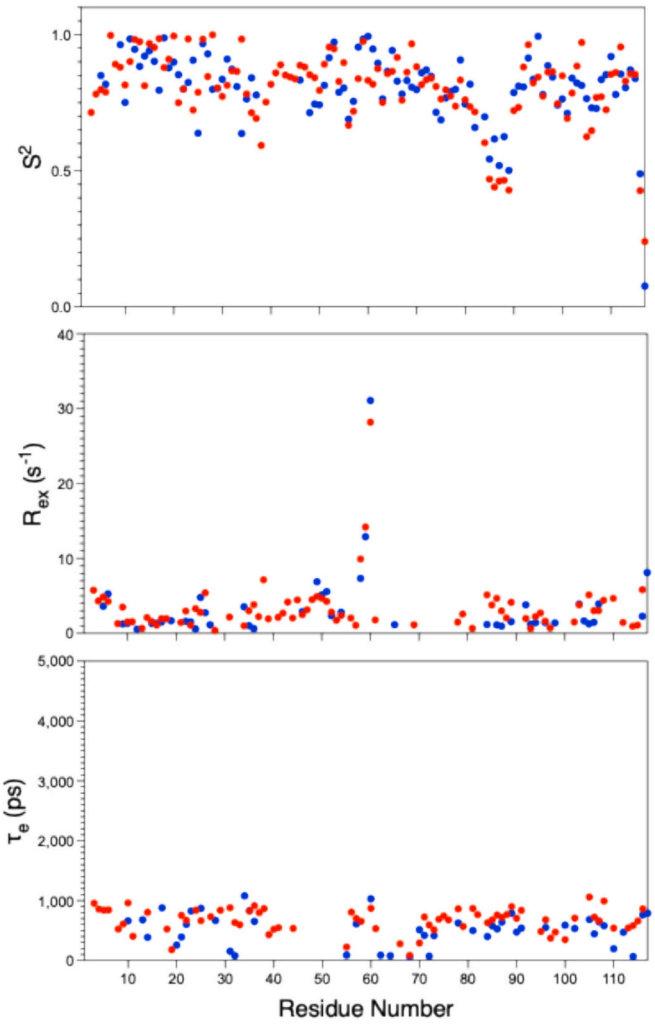

Fig. 4. Model-free parameters for Zn-*Hp*HypA (red) and Ni,Zn-*Hp*HypA (blue). Top: residue-wise backbone order parameters (S^2) reporting the amplitude of ps–ns internal motions. Middle: exchange contributions to transverse relaxation (R_{ex}, s^{-1}) reporting μs–ms dynamics Bottom: internal correlation times (τ_e, ps) for residues where inclusion of a fast internal timescale was supported by model selection. (For interpretation of the references to colour in this figure legend, the reader is referred to the web version of this article.)

$$c\left(s^{-2}\right) = \frac{\gamma_N^2 B_0^2 \Delta\sigma^2}{3} \tag{5}$$

Constants used in the relaxation calculations were: μ_0 = vacuum magnetic permeability = 4π x 10^{-7} T; $\hbar$ = reduced Planck constant = $1.0545718 \times 10^{-34}$ *J* s; γ_H = ^{1}H gyromagnetic ratio = $2.675221 \cdot 10^8$ T^{-1} s^{-1}; γ_N = ^{15}N gyromagnetic ratio = $-2.71262 \cdot 10^7$ T^{-1} s^{-1}; r_{NH} = N-H bond length = $1.02 \cdot 10^{-10}$ m; $\Delta\sigma$ = axially symmetric ^{15}N CSA = −172 ppm. The heteronuclear cross-correlation rate σ_{NH} (s^{-1}) depends only on d and $J(\omega_H \pm \omega_N)$ and therefore provides sensitivity to fast (ps–ns) N—H vector motions through the steady-state NOE: reduced σ_{NH} associated with increased ps–ns mobility yields lower NOE enhancements. The parameter that is normally used to report the heteronuclear "NOE" is actually (1 – NOE): if the N—H bond is rigid, the cross correlation rate σ_{NH} is more efficient, resulting in higher NOE values ($I \ll I_0$, $I/I_0 \ll 1$ and

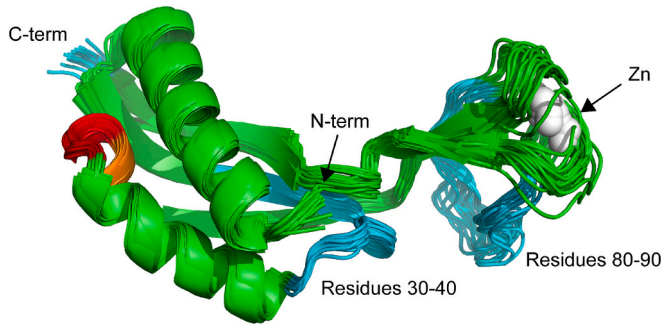

Fig. 5. Ribbon diagram of the NMR ensemble of Zn-*Hp*HypA (PDB code 6G81) colored according to the relaxation parameters (red: residues affected by a low $^{1}H—^{15}N$ HOE, orange: residues affected by conformational exchange and measurable R_2; cyan: residues affected by low S^2 values). The position of the N- and C-terms, as well as the Zn atoms are indicated. Figure made with PyMol 2.6.2 (The PyMOL Molecular Graphics System, Schrödinger, LLC). (For interpretation of the references to colour in this figure legend, the reader is referred to the web version of this article.)

"NOE" $\lesssim$1); if the N—H bond features mobility in the ps–ns timescale, the cross correlation rate σ_{NH} is less efficient, leading to a lower NOE value ($I < I_0, I/I_0 < 1$ and "NOE" < 1); if the N—H bond is highly flexible in this timescale, the NOE is further reduced ($I > I_0, I/I_0 > 1$, and "NOE" < 0).

Each spectral density $J(\omega)$ was modeled using Lorentzian terms describing overall tumbling and internal motion. This treatment yields the overall rotational correlation time τ_m, the effective correlation time τ_e for ps-ns internal motions, and the generalized order parameter (S^2), which reports the spatial restriction of the N—H bond vector. S^2 ranges from 1 for a rigid vector to 0 for complete disorder; in the cone model, $S = \frac{1}{2}(3cos^2\theta - 1)$. The relationships between the spectral density functions and the τ_m, τ_e, and S^2 parameters depend on the symmetry of the diffusion tensor (isotropic, axially symmetric or semi-isotropic, or anisotropic). For isotropic tumbling, the spectral density function is given by Eq. 6:

$$J(\omega_i) = \frac{2}{5}\left[\frac{S^2\tau_m}{\left[1+(\omega_i\tau_m)^2\right]} + \frac{(1-S^2)\tau_c}{\left[1+(\omega_i\tau_c)^2\right]}\right] \quad (6)$$

with $\tau_c^{-1} = \tau_m^{-1} + \tau_e^{-1}$. This expression can be extended [63] to include fast and slow internal motions with order parameters S_f and S_s (with $S^2 = S_f^2 \bullet S_s^2$, Eq. 7). For isotropic rotation, τ_m is related to the isotropic rotational diffusion coefficient D_r (s^{-1}) by $\tau_m = 1/(6D_r)$.

$$J(\omega) = \frac{2}{5}\cdot\left(\frac{S^2\tau_m}{1+(\omega\tau_m)^2} + \frac{\left(S_f^2 - S^2\right)\tau}{1+(\omega\tau)^2}\right) = \frac{2}{5}S_f^2\cdot\left(\frac{S_s^2\tau_m}{1+(\omega\tau_m)^2} + \frac{(1-S_s^2)\tau}{1+(\omega\tau)^2}\right) \quad (7)$$

Most proteins are not isotropic, and they tumble anisotropically by rotating along each axis with different correlation times. This behavior can be described by a diffusion tensor (a symmetric 3 × 3 matrix) with principal components D_{xx}, D_{yy}, and D_{zz} (with $D_{xx} \le D_{yy} \le D_{zz}$,) as diagonal elements [65]. In the fully anisotropic case, the spectral densities become weighted sums over five correlation times τ_j with weights A_j:

$$J(\omega_i) = \frac{2}{5}S_f^2\cdot\sum_{j=1}^{5}A_j\left(\frac{S_s^2\tau_j}{1+(\omega_i\tau_j)^2} + \frac{(1-S_s^2)\tau_j'}{1+\left(\omega_i\tau_j'\right)^2}\right) \quad (8)$$

where $\tau_j'^{-1} = \tau_j^{-1} + \tau_e^{-1}$ and the τ_j and A_j are combinations of D_{xx}, D_{yy}, D_{zz} [65]. The values of D_{xx}, D_{yy}, and D_{zz} determine the anisotropy and the rhombicity of the ellipsoid, so that if $D_{xx} \approx D_{yy} \le D_{zz}$ the tensor is axially symmetric, in which case the spectral density functions reduce to a sum over three terms:

$$J(\omega_i) = \frac{2}{5}S_f^2\cdot\sum_{j=1}^{3}A_j\left(\frac{S_s^2\tau_j}{1+(\omega_i\tau_j)^2} + \frac{(1-S_s^2)\tau_j'}{1+\left(\omega_i\tau_j'\right)^2}\right) \quad (9)$$

The diffusion tensor is additionally defined by the orientation of its principal axes (Euler angles) relative to a molecular reference frame, typically taken from an atomic structure [66]. Accordingly, extraction of τ_m, τ_e, and S^2, and R_{ex} from R_1, R_2 and NOE data requires determination of the rotational diffusion model and its tensor parameters.

Model-free analysis was performed in Dynamics Center 2.8.8 (Bruker) using the NOE/T_1/T_2 model-free module in a stepwise procedure. Rigid N—H vectors were first identified by excluding residues with NOE < 0.65 (fast local motions), residues showing evidence of conformational exchange (characterized by $T_2 < \overline{T_2} - \sigma$, where σ is the standard deviation), and residues affected by anisotropic tumbling (as diagnosed by $(T_2 - \overline{T_2})/T_2 > (T_1 - \overline{T_1})/T_1$) [56,66]. This selection yielded 56 and 41 residues for Zn-*Hp*HypA and Ni,Zn-*Hp*HypA, respectively. An initial isotropic τ_m value was then estimated by fitting R_2/R_1 ratios for these residues using simplified forms of the relaxation equations, neglecting R_{ex} and assuming that $J(\omega_i)$ depend only on isotropic tumbling [58]. The resulting isotropic τ_m values were 9.71 ± 0.77 ns for Zn-*Hp*HypA and 8.38 ± 0.61 ns for Ni,Zn-*Hp*HypA. These values were used as starting guesses for fitting the diffusion tensor, which requires knowledge of N—H bond orientations; these were derived from the medoid NMR structure of Zn-*Hp*HypA [31]. The tensor parameters (D_{xx}, D_{yy}, D_{zz} and Euler angles) were optimized by minimizing the discrepancy between observed and predicted R_2/R_1 ratios. The principal diffusion components and derived quantities are reported in Table 1 and indicate a prolate diffusion tensor for both protein forms, consistent with the solution structure [31].

The diffusion tensor parameters thus obtained were used to perform residue-specific fits to R_1, R_2, and NOE using the tensor model-free models implemented in Dynamics Center (TM1-TM5), which differ in the internal motions terms included: TM1 fits S^2 only; TM2 fits S^2 and τ_e; TM3 fits S^2 and R_{ex}; TM4 uses S^2, τ_e, and R_{ex}; TM5 is an extended model in which internal motion is represented by a fast component (S_f^2, with τ_f approximated to zero) and a slower component described by S^2 and τ_s. Because the correlation times τ_j are linear combinations of the diffusion tensor components, these residue-specific fits also refine the diffusion tensor. For each residue, Dynamics Center attempted all TM1–TM5 fits and rejected failed optimizations or non-physical solutions (*e.g.*, $0 \le S^2 \le 1$, non-negative R_{ex}, or violations of constraints such as $S_f^2 \ge S^2$ for TM5). Dynamics Center thus reported a residue-specific Akaike Information Criterion (AIC) value for each candidate model; however, because AIC can be strongly influenced by experimental uncertainties (particularly by errors in NOE values), a conservative model-selection procedure was applied that combined the AIC with Dynamics Center's asterisk fit-quality indicator. Specifically, when one or more models were marked with an asterisk (indicating that the fitted R_1 and R_2 values reproduced experimental values within 2% error) the selected model was the simplest among the starred solutions (*i.e.*, TM1 preferred over TM2/TM3, and TM2/TM3 preferred over TM4/TM5); ties were resolved by choosing the lower AIC within that subset. If no starred model was available, the minimum-AIC model was identified, and the final choice was taken as the simplest model within ΔAIC ≤2 of that minimum. Model-free parameters

were extracted from the selected model for each residue; S^2 was obtained for all successful fits, whereas R_{ex} and τ_e were available only when included in the selected model (TM3/TM4 for R_{ex}; TM2/TM4 for τ_e). The resulting residue-wise parameters were assembled for Zn-*Hp*HypA and Ni,Zn-*Hp*HypA and plotted as functions of residue number to visualize changes in backbone dynamics upon Ni(II) binding (Fig. 4).

3. Results

The availability of the assignments of $^{1}H,^{15}N$ HSQC spectra for both Zn-*Hp*HypA (Fig. 2) and its holo-form Ni,Zn-*Hp*HypA [31] enabled a residue-specific comparison of the backbone dynamics in the two metalation states. Backbone ^{15}N R_1, R_2, and NOE values at 16.4 T for Zn–*Hp*HypA and Ni,Zn–*Hp*HypA are shown in Fig. 3. Relaxation parameters were determined for 114 residues in the apo-protein and 102 residues in the holo-protein. Resonances near the Ni(II) site in the holo-protein were broadened beyond detection, consistent with paramagnetic relaxation enhancement as previously reported [31].

A qualitative inspection of the relaxation profiles (Fig. 3) allowed the identification of global trends and localized dynamic features (Fig. 5). For Zn-*Hp*HypA, the mean NOE values 0.70 ± 0.09 indicate a largely rigid backbone on the ps-ns timescale. As expected, substantially reduced NOEs are observed at the C-terminal tail, consistent with enhanced flexibility. Additional regions of reduced NOEs include residues 55–60 (connecting helix α2 to strand β2), and residues 81–93 (the long loop between strand β4 and strand β5), suggesting localized fast dynamics in these segments. These flexible regions are also present in Ni, Zn-*Hp*HypA, which displays essentially invariant mean NOEs (0.70 ± 0.10), indicating that Ni(II) binding does not significantly affect fast backbone mobility. Across most of the sequence, R_1 values are relatively uniform in both metalation states, consistent with a dominant contribution from overall tumbling. In Zn-*Hp*HypA (mean $R_1 = 1.22 \pm 0.13$ s^{-1}), helix α2 (residues 41–54) shows slightly reduced R_1 values relative to the mean, suggestive of a locally more restricted backbone; this region is not observable in Ni,Zn–*Hp*HypA (mean $R_1 = 1.29 \pm 0.12$ s^{-1}) due to Ni-induced line broadening. R_2 values (mean $R_2 = 15.4 \pm 3.6$ and 13.3 ± 4.1 s^{-1} for apo and holo protein) are similarly broadly uniform across the protein sequence in both Zn- and Ni,Zn-*Hp*HypA. Consistently, most residues display relatively uniform values of the R_2/R_1 ratio along the sequence (mean $R_2/R_1 = 12.8 \pm 3.4$ and 10.4 ± 3.4 for apo and holo *Hp*HypA, respectively), again indicative of relaxation dominated by overall tumbling and local fast motions. However, the region spanning residues 58–60, linking helix α2 and strand β2 (Fig. 5), displays significantly high values of R_2 and R_2/R_1 in both metalation states, indicating the presence of significant exchange contributions on the μs–ms timescale to R_2. Remarkably, residues 68–71 and 102–106, which connect the nickel-binding and zinc-binding domains, do not show anomalies in the relaxation parameters, suggesting the absence of large-amplitude interdomain motions within the sensitivity of these experiments. Overall, the qualitative relaxation profiles show similar average fast backbone mobility on the ps–ns timescale; the slightly higher mean R_1 as well as lower mean R_2 and R_2/R_1 in the holo protein suggest that Ni,Zn-*Hp*HypA experiences less slow conformational exchange and/or faster overall rotational diffusion than the apo state.

To define the effects of Ni(II) binding on the solution backbone dynamics of *Hp*HypA, the ^{15}N relaxation data were quantitatively analyzed by expressing the relaxation rates within the Abragam–Redfield treatment of ^{15}N relaxation [64] and modeling bond-vector dynamics with the Lipari–Szabo model-free formalism [53,62,63]. The obtained parameters are shown in Fig. 4. For both metalation states, the protein remains globally well-ordered on the ps–ns timescale, as shown by the predominantly high backbone order parameters S^2 values across most of the sequence (0.81 ± 0.13 for both apo and holo *Hp*HypA). The two states display broadly similar dynamic profiles, with mobility confined to a few localized regions. Reduced S^2 values are observed in selected segments, particularly around residues ~30–40, ~80–90, and at the C-terminus, describing enhanced local flexibility in both states (Fig. 5). The corresponding internal correlation times, τ_e, are generally in the few-hundred-picoseconds range, consistent with restricted fast internal motions rather than extensive disorder. A distinct feature of the model-free analysis is the presence of conformational exchange contributions in the μs–ms regime in a region centered around residue ~60 in both forms (Fig. 5).

These results indicate that the effect of Ni(II) binding on ps-ns backbone flexibility is limited. On the other hand, the refined rotational diffusion tensor parameters derived from this analysis, reported in Table 1, indicate that Ni,Zn-*Hp*HypA tumbles significantly faster than Zn-*Hp*HypA. In particular, all the principal components of the diffusion tensor increase upon Ni(II) binding and, accordingly, the isotropic average diffusion coefficient increases concomitantly with a decrease of the overall correlation time. The effective hydrodynamic volume and radius derived from the tensor consequently decrease in the holo state. By contrast, the diffusion anisotropy remains essentially invariant, while the rhombicity increases, indicating that Ni(II) binding affects the detailed distribution of mass and/or shape without substantially altering the overall degree of anisotropy. These data suggest that Ni(II) binding shifts Zn-*Hp*HypA to a faster tumbling and more compact solution state, while preserving the overall backbone internal dynamic behavior.

The *ca.* 15% estimated increase of the rotational diffusion coefficient of Zn-*Hp*HypA upon Ni(II) binding, and the corresponding decrease in τ_m, suggests a reduced effective hydrodynamic radius R_h for the holo state. As a first approximation, a ratio $R_h^{holo}/R_h^{apo} \approx 0.96$ can be inferred from D_r using the Stokes-Einstein-Debye eq. [67]:

$$D_r = k_B T / 8\pi\eta R_h^3 \tag{11}$$

This value is consistent with the ratio of the hydrodynamic radii (0.94) reported in Table 1.

Table 1
Diffusion tensor parameters for apo and holo *Hp*HypA.

	Zn-*Hp*HypA	Zn,Ni-*Hp*HypA
D_{xx} (MHz)	14.8 ± 0.1	16.6 ± 0.2
D_{yy} (MHz)	15.8 ± 0.1	18.3 ± 0.2
D_{zz} MHz)	20.5 ± 0.1	23.7 ± 0.2
Anisotropy[a]	1.34	1.36
Rhombicity[b]	0.29	0.41
D_r (MHz)[c]	17.0	19.5
τ_m (ns)[d]	9.80	8.55
Volume (V, $s^{3/2}$)[e]	6.05×10^{-11}	4.94×10^{-11}
Radius (R, $s^{1/2}$)[f]	2.43×10^{-4}	2.28×10^{-4}

[a] $Anisotropy = \dfrac{2D_{zz}}{D_{xx}+D_{yy}}$.

[b] $Rhombicity = \dfrac{\frac{3}{2}(D_{yy}-D_{xx})}{D_{zz}-\frac{1}{2}(D_{xx}+D_{yy})}$.

[c] $D_r = \dfrac{D_{xx}+D_{yy}+D_{zz}}{3}$.

[d] $\tau_m = \dfrac{1}{6D_r}$.

[e] $V = \dfrac{4}{3}\pi\dfrac{1}{\sqrt{D_{xx}}}\dfrac{1}{\sqrt{D_{yy}}}\dfrac{1}{\sqrt{D_{zz}}}$.

[f] $R = \sqrt[3]{\dfrac{3}{4}\dfrac{V}{\pi}}$.

4. Discussion

Nickel trafficking in *Helicobacter pylori* must satisfy competing constraints: Ni(II) must be bound strongly enough to avoid adventitious sequestration or toxicity, yet the carrier must remain sufficiently dynamic to exchange partners and deliver the metal ion to the maturation pathways of urease and [Ni,Fe]-hydrogenase. *Hp*HypA operates at the intersection of these requirements, coupling metal binding to protein-protein recognition to direct Ni(II) toward downstream partner chaperones such as the urease chaperone $UreE_2$ or the [Ni,Fe]-hydrogenase large subunit HyhL, which ultimately support activation of the respective enzymes [10]. The central conclusion of this work is that Ni(II) binding shifts the conformational ensemble of Zn-*Hp*HypA toward a measurably more compact solution state, as indicated by the increase in the rotational diffusion coefficients. In contrast, residue-resolved model-free parameters are overall similar in the apo and holo forms, indicating that Ni loading does not broadly reorganize ps–ns internal backbone dynamics.

The thermodynamic behavior of the *Hp*HypA–$UreE_2$ system provides a complementary framework for interpreting these observations [32]. Calorimetric measurements (Table 2) show that Ni(II) binding to Zn-*Hp*HypA is relatively weak and associated with a modest enthalpic term and a large favorable entropy term, whereas Ni(II) binding to *Hp*$UreE_2$ is strongly enthalpy-driven and entropically disfavored. Zn-*Hp*HypA and *Hp*$UreE_2$ form a micromolar Zn-*Hp*HypA•*Hp*$UreE_2$ complex in the absence of Ni(II), while Ni(II) enables a much tighter ternary Ni,Zn-*Hp*HypA•*Hp*$UreE_2$ complex whose stabilization is dominated by a large favorable enthalpy and accompanied by a reduced favorable entropy contribution. The entropy term from ITC reflects the net balance of translational/rotational, solvation, and conformational components. Within this context, the NMR evidence is consistent with a scenario in which Ni(II) modifies the ensemble toward more compact states and facilitates a recognition geometry that, upon complex formation, can yield a large enthalpic gain, particularly if Ni(II) participates in a shared coordination environment at the interface as previously proposed [32]; concomitantly, the overall entropy term becomes less favorable because the ternary complex imposes stricter geometric constraints and reduces the number of accessible interfacial microstates.

This interpretation corroborates the rotational diffusion and calorimetry data: if Ni(II) shifts Zn-*Hp*HypA toward more compact conformers, partner encounters may occur from a narrower set of starting geometries, increasing the probability of productive complex formation without requiring large changes in ps–ns backbone mobility. At the same time, once the metal-bridged complex forms, the directional and highly constrained coordination chemistry can optimize packing and electrostatics at the interface, driving a large negative ΔH. The same constraints that improve enthalpy, namely tight coordination and optimized contact geometry, can reduce configurational freedom at the interface and decrease solvent-entropy gains, producing the characteristic enthalpy/entropy repartitioning often observed for metal-locked complexes. In this view, Ni(II) provides specificity and directionality not merely through affinity gradients between isolated sites, but by stabilizing a distinct intermediate state with a large enthalpic payoff.

Comparable behavior has been documented for Cu(I) trafficking [34–37]. Although Ni(II) and Cu(I) coordination chemistry differs, the shared principle is that the metal participates directly in assembling a productive interprotein state rather than behaving as a freely diffusing ligand exchanged between independent sites. Notably, a closely analogous Ni(II)-triggered allosteric response has been recently described for the *H. pylori* Ni(II)-responsive transcription factor NikR: ^{19}F NMR spectroscopic evidence [38] and follow-up mechanistic work [39] showed that Ni(II) binding to apo-*Hp*NikR induces an allosteric effect that quenches protein mobility and shifts a conformational equilibrium toward a DNA-binding and more rigid competent state, mirroring the Ni(II)-dependent ensemble narrowing observed here for HypA samples.

A plausible structural basis for the increased compactness in the holo-state of *Hp*HypA may lie in the architecture of the Ni(II)-binding site: the metal coordination sphere involves the N-terminal amine N atom of Met1, the deprotonated backbone amide N atoms of His2 and Glu3, the imidazole Nδ atom of His2, one carboxylate O atom of Glu3, and therefore the so-called MHE motif. Critically, coordination also includes one Oδ atom from the sidechain carboxylate of Asp40 [31], which is positioned at the C-terminal end of helix α2 and faces helix α1 (Fig. 1). This latter interaction could be responsible for a tighter packing of helices α1 and α2, providing a structural rationale for the reduced hydrodynamic radius and volume observed for the holo protein. The finding that global compaction occurs with only modest changes in residue-level ps–ns dynamics is consistent with a packing effect that alters inter-helical geometry and overall shape rather than suppressing fast backbone fluctuations.

These results have implications for the handoff mechanism within the *Hp*HypA•*Hp*$UreE_2$ network. This mechanism must involve breaking the metal-bridge between *Hp*HypA and *Hp*$UreE_2$, reported to include the two conserved His102A and His102B on adjacent monomers of *Hp*$UreE_2$ [32] in addition to the MHE motif of *Hp*HypA, and shifting Ni(II) to a *Hp*$UreE_2$-only coordination mode, which has been shown to include His102A and His102B as well as His152A and His152B, positioned on the long C-terminal tails of the homodimer [68]. This process might freeze the latter in a conformation that disfavors binding to HypA, while at the same time increase conformational flexibility in *Hp*HypA, with consequent entropy increase that would support the release of apo-*Hp*HypA. The large stability of the Ni-*Hp*HypA•*Hp*$UreE_2$ ternary complex suggests that nickel transfer is unlikely to be governed by simple dissociation from *Hp*HypA followed by capture by *Hp*$UreE_2$. Instead, transfer may require coupling to additional events that move the pathway forward, such as engagement of *Hp*$UreE_2$ with downstream components (*e.g.*, *Hp*UreG) that effectively pull Ni(II) toward the next maturation step [10,23].

CRediT authorship contribution statement

Stefano Ciurli: Writing – review & editing, Writing – original draft, Methodology, Investigation, Funding acquisition, Formal analysis, Data curation, Conceptualization. **Luca Mazzei:** Writing – review & editing, Supervision, Methodology. **Barbara Zambelli:** Writing – review & editing, Supervision, Methodology. **Sofia Ranieri:** Writing – review & editing, Methodology. **Noemi Carosella:** Writing – review & editing, Methodology. **Massimo Lucci:** Writing – review & editing,

Table 2
Calorimetric data of *Hp*HypA, *Hp*$UreE_2$ and Ni(II) binding [32].

	Zn-*Hp*HypA + Ni(II)	*Hp*$UreE_2$ + Ni(II)	Zn-*Hp*HypA + *Hp*$UreE_2$	Ni,Zn-*Hp*HypA + *Hp*$UreE_2$
K_D	0.90 ± 0.04 μM	0.294 ± 0.09 μM	0.84 ± 0.01 μM	0.15 ± 0.09 nM
ΔH (kcal mol^{-1})	−0.83 ± 0.02	−11.58 ± 0.03	−6.33 ± 0.01	−12.42 ± 0.02
ΔS (cal mol^{-1} K^{-1})	+24.9	−8.98	+6.56	+3.22
ΔG (kcal mol^{-1})	−8.23 ± 0.03	−8.91 ± 0.03	−8.28 ± 0.02	−13.38 ± 0.03

Methodology. **Frans A.A. Mulder:** Writing – review & editing, Methodology, Conceptualization.

Declaration of competing interest

The authors declare the following financial interests/personal relationships which may be considered as potential competing interests:

Given his role as the Editori-in-Chief of the J. Inorg. Biochem., Stefano Ciurli has had no involvement in the peer review of this article, and had no access to information regarding its peer review. Full responsibility for the editorial process for this article was delegated to another journal editor. All other authors declare that they have no known competing financial interests or personal relationships that could have appeared to influence the work reported in this paper.

Acknowledgements

Part of this research was facilitated by a Research Fellowship to S.C. awarded by Johannes Kepler University. L.M., B.Z., S.R., N.C. and S.C. acknowledge support by the University of Bologna and the Consorzio Interuniversitario di Risonanze Magnetiche di Metallo-Proteine (CIRMMP). Silvia Biolcati is thanked for help in protein purification.

This paper contributes to a collection of works honoring the 90th birthday of Professor H. B. Gray, a pioneer in bioinorganic chemistry and an outstanding scientist. I, S.C., personally regret that circumstances did not allow me to work with him when the opportunity arose, as it would have been a privilege to learn directly from such an inspiring figure in our field. Nevertheless, Harry has been a constant source of inspiration throughout my scientific career, and I have long regarded him as a mentor from afar.

References

[1] S.L. Benoit, E.F. Miller, R.J. Maier, Infect. Immun. 81 (2013) 580–584.
[2] B. Zambelli, S. Ciurli, Met. Ions Life Sci. 13 (2013) 321–357.
[3] K.P. Haley, J.A. Gaddy, Gastroenterol. Res. Pract. 2016 (2016) 3019362–3019410.
[4] F. Fischer, M. Robbe-Saule, E. Turlin, F. Mancuso, V. Michel, P. Richaud, F. J. Veyrier, H. De Reuse, D. Vinella, PLoS Pathog. 12 (2016) e1006018.
[5] B. Zambelli, V.N. Uversky, S. Ciurli, BBA Proteins Proteom. 1864 (2016) 1714–1731.
[6] A.H. van Vliet, E.J. Kuipers, B. Waidner, B.J. Davies, N. de Vries, C.W. Penn, C. M. Vandenbroucke-Grauls, M. Kist, S. Bereswill, J.G. Kusters, Infect. Immun. 69 (2001) 4891–4897.
[7] J.W. Olson, R.J. Maier, Science 298 (2002) 1788–1790.
[8] K. Stingl, H. De Reuse, Int. J. Med. Microbiol. 295 (2005) 307–315.
[9] A.W. Debowski, S.M. Walton, E.-G. Chua, A.C.-Y. Tay, T. Liao, B. Lamichhane, R. Himbeck, K.A. Stubbs, B.J. Marshall, A. Fulurija, M. Benghezal, in: L.D. Simon (Ed.), PLoS Pathog 13, 2017, p. e1006464.
[10] M.J. Maroney, S. Ciurli, Semin. Cancer Biol. 76 (2021) 143–155.
[11] C.J. Zeer-Wanklyn, D.B. Zamble, Curr. Opin. Chem. Biol. 37 (2017) 80–88.
[12] J.W. Olson, N.S. Mehta, R.J. Maier, Mol. Microbiol. 39 (2001) 176–182.
[13] N. Mehta, J.W. Olson, R.J. Maier, J. Bacteriol. 185 (2003) 726–734.
[14] S.L. Benoit, N. Mehta, M.V. Weinberg, C. Maier, R.J. Maier, Microbiology 153 (2007) 1474–1482.
[15] B. Zambelli, F. Musiani, S. Benini, S. Ciurli, Acc. Chem. Res. 44 (2011) 520–530.
[16] H. de Reuse, D. Vinella, C. Cavazza, Front. Cell. Infect. Microbiol. 3 (2013) 1–6.
[17] F. Musiani, B. Zambelli, M. Bazzani, L. Mazzei, S. Ciurli, Metallomics 7 (2015) 1305–1318.
[18] C. Tarsia, A. Danielli, F. Florini, P. Cinelli, S. Ciurli, B. Zambelli, Biochim. Biophys. Acta Gen. Subj. 1862 (2018) 2245–2253.
[19] Y.S. Nim, K.-B. Wong, Inorganics 7 (2019) 85.
[20] K. Higgins, Inorganics 7 (2019) 104.
[21] R. Maier, S.L. Benoit, Inorganics 7 (2019) 80–131.
[22] B. Zambelli, L. Mazzei, S. Ciurli, Prog. Mol. Biol. Transl. Sci. 174 (2020) 307–330.
[23] Y.S. Nim, I.Y.H. Fong, J. Deme, K.L. Tsang, J. Caesar, S. Johnson, L.T.H. Pang, N.M. H. Yuen, T.L.C. Ng, T. Choi, Y.Y.H. Wong, S.M. Lea, K.-B. Wong, Sci. Adv. 9 (2023) pp. eadf7790.
[24] N. Carosella, K.P. Brock, B. Zambelli, F. Musiani, C. Sander, S. Ciurli, Front. Chem. Biol. 2 (2023) 1243564.
[25] J.A. Hernandez, P.S. Micus, S.A.L. Sunga, L. Mazzei, S. Ciurli, G. Meloni, Chem. Sci. 15 (2024) 651–665.
[26] S.L. Benoit, J.L. McMurry, S.A. Hill, R.J. Maier, Biochim. Biophys. Acta 1820 (2012) 1519–1525.
[27] H.Q. Hu, R.C. Johnson, D.S. Merrell, M.J. Maroney, Biochemistry 56 (2017) 1105–1116.
[28] F.C. Blum, H.Q. Hu, S.L. Servetas, S.L. Benoit, R.J. Maier, M.J. Maroney, D. S. Merrell, in: C. Eric (Ed.), PLoS One 12, 2017, p. e0183260.
[29] W. Xia, H. Li, K.-H. Sze, H. Sun, J. Am. Chem. Soc. 131 (2009) 10031–10040.
[30] R.C. Johnson, H.Q. Hu, D.S. Merrell, M.J. Maroney, Metallomics 7 (2015) 674–682.
[31] C. Spronk, S. Zerko, M. Gorka, W. Kozminski, B. Bardiaux, B. Zambelli, F. Musiani, M. Piccioli, P. Basak, F.C. Blum, R.C. Johnson, H. Hu, D.S. Merrell, M. Maroney, S. Ciurli, J. Biol. Inorg. Chem. 23 (2018) 1309–1330.
[32] B. Zambelli, P. Basak, H. Hu, M. Piccioli, F. Musiani, V. Broll, L. Imbert, J. Boisbouvier, M.J. Maroney, S. Ciurli, Metallomics 15 (2023) mfad003.
[33] E.F. Pettersen, T.D. Goddard, C.C. Huang, G.S. Couch, D.M. Greenblatt, E.C. Meng, T.E. Ferrin, J. Comput. Chem. 25 (2004) 1605–1612.
[34] A. Rodriguez-Granillo, P. Wittung-Stafshede, J. Phys. Chem. B 112 (2008) 4583–4593.
[35] M.S. Niemiec, C.F. Weise, P. Wittung-Stafshede, PloS One 7 (2012) e36102.
[36] M.S. Niemiec, A.P.G. Dingeldein, P. Wittung-Stafshede, Sci. Rep. 5 (2015) 10518.
[37] O. Perkal, Z. Qasem, M. Turgeman, R. Schwartz, L. Gevorkyan-Airapetov, M. Pavlin, A. Magistrato, D.T. Major, S. Ruthstein, J. Phys. Chem. B 124 (2020) 4399–4411.
[38] K.A. Baksh, D. Pichugin, R.S. Prosser, D.B. Zamble, J. Biol. Chem. 296 (2021) 100069.
[39] K.A. Baksh, J. Augustine, A. Sljoka, R.S. Prosser, D.B. Zamble, J. Biol. Chem. (2022) 102785.
[40] D.D. Boehr, R. Nussinov, P.E. Wright, Nat. Chem. Biol. 5 (2009) 789–796.
[41] D.A. Capdevila, J.J. Braymer, K.A. Edmonds, H. Wu, D.P. Giedroc, Proc. Natl. Acad. Sci. U. S. A. 114 (2017) 4424–4429.
[42] D.A. Capdevila, K.A. Edmonds, G.C. Campanello, H. Wu, G. Gonzalez-Gutierrez, D. P. Giedroc, J. Am. Chem. Soc. 140 (2018) 9108–9119.
[43] A. Mittermaier, L.E. Kay, Science 312 (2006) 224–228.
[44] K. Henzler-Wildman, D. Kern, Nature 450 (2007) 964–972.
[45] N.E. Grossoehme, D.P. Giedroc, J. Am. Chem. Soc. 131 (2009) 17860–17870.
[46] A.J. Wand, Curr. Opin. Struct. Biol. 23 (2013) 75–81.
[47] K.A. Sharp, E. O'Brien, V. Kasinath, A.J. Wand, Proteins 83 (2015) 922–930.
[48] J.A. Caro, K.W. Harpole, V. Kasinath, J. Lim, J. Granja, K.G. Valentine, K.A. Sharp, A.J. Wand, Proc. Natl. Acad. Sci. U. S. A. 114 (2017) 6563–6568.
[49] L.E. Kay, Nat. Struct. Biol. 5 (Suppl) (1998) 513–517.
[50] A.G.I. Palmer, Chem. Rev. 104 (2004) 3623–3640.
[51] M.A. Stetz, J.A. Caro, S. Kotaru, X. Yao, B.S. Marques, K.G. Valentine, A.J. Wand, in: A.J. Wand (Ed.), Methods Enzymol. 615, Academic Press, 2019, pp. 237–284.
[52] M.P. Williamson, Prog. Nucl. Magn. Reson. Spectrosc. 73 (2013) 1–16.
[53] G. Lipari, A. Szabo, J. Am. Chem. Soc. 104 (1982) 4546–4559.
[54] N.A. Farrow, R.R. Muhandiram, A.U. Singer, S.M. Pascal, C.M. Kay, G.G. Gish, S. E. Shoelson, T.T. Pawson, J.D. Forman-Kay, L.E.L. Kay, Biochemistry 33 (1994) 5984–6003.
[55] C. Charlier, S.F. Cousin, F. Ferrage, Chem. Soc. Rev. 45, The Royal Society of Chemistry, 2016, pp. 2410–2422.
[56] N. Tjandra, S.E. Feller, R.W. Pastor, A. Bax, J. Am. Chem. Soc. 117 (1995) 12562–12566.
[57] L.K. Lee, M. Rance, W.J. Chazin, A.G. Palmer III, J. Biomol. NMR 9 (1997) 287–298.
[58] L.E. Kay, D.A. Torchia, A. Bax, Biochemistry 28 (1989) 8972–8979.
[59] I. Palmer, A.G. Curr, Opin. Biotechnol. 4 (1993) 385–391.
[60] M. Stola, F. Musiani, S. Mangani, P. Turano, N. Safarov, B. Zambelli, S. Ciurli, Biochemistry 45 (2006) 6495–6509.
[61] T. Stief, K. Vormann, N.A. Lakomek, J. Vis. Exp. 213 (2024) 1–31.
[62] G. Lipari, A. Szabo, J. Am. Chem. Soc. 104 (1982) 4559–4570.
[63] G.M. Clore, A. Szabo, A. Bax, L.E. Kay, P.C. Driscoll, A.M. Gronenborn, J. Am. Chem. Soc. 112 (1990) 4989–4991.
[64] A. Abragam (Ed.), The Principles of Nuclear Magnetism, Clarendon Press, Oxford, 1961.
[65] D.E. Woessner, J. Chem. Phys. 37 (1962) 647–654.
[66] R. Ghose, D. Fushman, D. Cowburn, J. Magn. Reson. 149 (2001) 204–217.
[67] S. Yao, D.W. Keizer, J.J. Babon, F. Separovic, Eur. Biophys. J. 51 (2022) 193–204.
[68] K. Banaszak, V. Martin-Diaconescu, M. Bellucci, B. Zambelli, W. Rypniewski, M. J. Maroney, S. Ciurli, Biochem. J. 441 (2012) 1017–1026.